

Lie-Group Theoretic Approach to Shape-Sensing Using FBG-Sensorized Needles Including Double-Layer Tissue and S-Shape Insertions

Dimitri A. Lezcano^{ID}, Iulian I. Iordachita^{ID}, Senior Member, IEEE, and Jin Seob Kim^{ID}, Member, IEEE

Abstract—Flexible bevel-tipped needles are often used for needle insertion in minimally invasive surgical techniques due to their ability to be steered in cluttered environments. Shape-sensing enables physicians to determine the location of needles intraoperatively without requiring radiation of the patient, enabling accurate needle placement. In this article, we validate a theoretical method for flexible needle shape-sensing that allows for complex curvatures, extending upon a previous sensor-based model. This model combines curvature measurements from fiber-Bratt grating (FBG) sensors and the mechanics of an inextensible elastic rod to determine and predict the 3-D needle shape during insertion. We evaluate the model's shape sensing capabilities in C- and S-shaped insertions in single-layer isotropic tissue, and C-shaped insertions in two-layer isotropic tissue. Experiments on a four-active area, FBG-sensorized needle were performed in varying tissue stiffnesses and insertion scenarios under stereo vision to provide the 3-D ground truth needle shape. The results validate a viable 3-D needle shape-sensing model accounting for complex curvatures in flexible needles with mean needle shape-sensing root-mean-square errors (RMSEs) of 0.160 ± 0.055 mm over 650 needle insertions.

Index Terms—Fiber optics, fiber-Bratt grating, flexible needle, lie-group, medical device, shape-sensing.

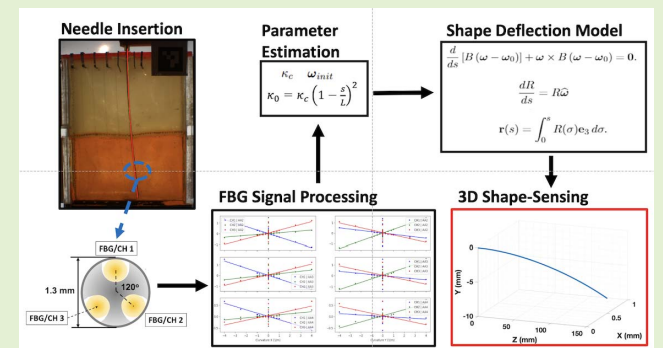
I. INTRODUCTION

N EEDLE insertion is a typical minimally invasive surgical technique in procedures like biopsy, drug-delivery, and cryoablation. Particularly, prostate surgical interventions are required for patients who have prostate cancer, a significant and potentially fatal disease for men. On average, 1.6 million men are diagnosed with prostate cancer and over 350 000 men die of prostate cancer [1]. Procedures like prostate biopsy and prostate cryoablation enable physicians to adequately treat those with prostate cancer, both requiring for needle insertion into the prostate. However, needle insertion can cause significant tissue damage due to needle readjustments and reinsertions to properly place the needle at the target location [2].

Manuscript received 21 September 2022; accepted 23 September 2022. Date of publication 11 October 2022; date of current version 14 November 2022. This work was supported by the National Institutes of Health under Grant R01CA235134. The associate editor coordinating the review of this article and approving it for publication was Dr. Ioannis Raptis. (*Corresponding author: Dimitri A. Lezcano.*)

The authors are with the Mechanical Engineering Department, Johns Hopkins University, Baltimore, MD 21201 USA (e-mail: dlezcan1@jhu.edu; iordachita@jhu.edu; jkim115@jhu.edu).

Digital Object Identifier 10.1109/JSEN.2022.3212209



Furthermore, sensitive anatomical structures like the bladder and vascular structures create difficulty in properly inserting the needle into the prostate and require complex insertion avoidance maneuvers [2]. Asymmetric flexible bevel-tipped needles have become a common tool for needle insertions as they naturally bend and can be used to steer during insertion, reducing the surgeon's need to readjust the needle, thus reducing tissue damage. However, accurate determination of the needle's position in the patient is required to properly insert these needles to reach the prostate.

Robotic and automatic technologies for needle insertion have been researched since the mid-2000s. The focus of this research is to achieve accurate needle positioning during insertion through either smart operation of flexible needles, intelligent-sensing embedded into flexible needles, or a combination of the two. Needle insertion technology research has ranged from the design and evaluation steerable flexible needles using actuated inner stylets and needle tips [3], [4], [5], passive needle steering [6], [7], [8], [9], [10], motion planning methods for insertion planning [11], [12], [13], [14], [15], [16], [17], [18], and shape-sensing and tracking methods intraoperatively [19], [20], [21], [22], [23]. For needle tracking,

several techniques have been used such as MRI [14], [20], ultrasound [5], [7], CT or fluoroscopy [9], [24], electromagnetic sensors [25], and fiber-Bragg grating (FBG) sensors [26]. Among these techniques, we are particularly interested in FBG sensing for its viability for MR imaging and real-time sensing capabilities.

To equip surgeons with the capability to maneuver flexible needles, shape-sensing techniques in flexible needles have been well-researched over the past few decades. Research began with simple kinematic models like the unicycle and bicycle models for needle shape-sensing and steering [8], [11]. Secoli and Rodriguez y Baena [27] estimated the 3-D shape of the needle and performed closed-loop control through extending the bicycle model and nonholonomic dynamics of needle steering. These models are lightweight and well-described, however, are limited in the realization of the needle's shape due to the constant curvature assumption. More complex models have included mechanics-based models founded on classical beam theory have been used to address this issue, but typically require detailed tissue information that may not be able to determine or change preoperatively and intraoperatively [28], [29], [30]. A Lie-group theoretic model that utilizes a sensor-based approach has been developed to provide accurate shape-sensing and allow for complex 3-D shape modeling. This model allows for 3-D curvatures, is independent of preoperative tissue information and leverages the natural bend of flexible needles sensorized with FBG sensors to provide shape-sensing flexibility [31], [32]. Founded upon elastic rod theory, this model utilizes Lie groups to enable 3-D needle shape-sensing through FBG-based strain sensing.

Previous works in shape-sensing have utilized single-core FBGs and multicore FBGs (MCFs) for measuring curvature and strain of flexible needles and catheters. A flexible nitinol needle embedded with single-core FBG arrays demonstrated needle shape-sensing in free-space and gelatin phantom using kinematic constant curvature modeling and 3-D space curves [26], [33]. Single-core FBG-sensorized needles have been used for passive needle steering using constant-curvature modeling with mechanics-based shape-sensing [34]. Active needle steering through tendon-driven bevel-tip directioning was demonstrated for controlling needle deflection in gelatin phantoms leveraging constant-curvature modeled shape-sensing [35]. Catheters embedded with an MCF were evaluated for free-space shape-sensing using 3-D space-curves for vascular catheterization procedures [36], [37]. 3-D catheter shape-sensing via 3-D space curves was extended using Bishop frames to determine needle position and orientation and allowing for curvature discontinuities along the catheter [38]. This system was further extended using biplane fluoroscopy to fuse into the sensorized catheter's shape-sensing capabilities for enhancing catheter shape-reconstruction methods, allowing for distinguishing between bending and twisting strain [39]. An MCF-sensorized catheter instrumented with EM sensors was demonstrated for endovascular navigation registering the 3-D sensed catheter shape from space curve shape-sensing into a CT coordinate system using the EM sensors and metallic markers for free-space bending and navigation through a 3-D-printed

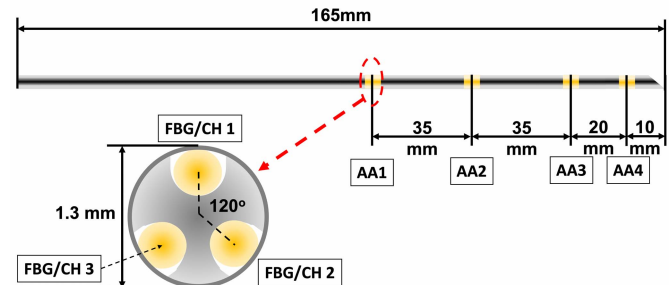


Fig. 1. Four active area sensorized-needle configuration used in these experiments. Top: Sensor locations along the sensorized-needle. Bottom-left: Cross section of the needle with the fiber-optic sensors (in yellow) in a triangular layout.

vascular phantom [40], [41]. An epidural needle instrumented with four nanoparticle-doped single-core fibers have been evaluated for shape-sensing accuracy using distributed sensing and kinematic shape-modeling in phantom epidural insertion experiments [42]. Kalman-filtering shape-estimation methods demonstrated dynamic 3-D shape-sensing using single-core fibers with sparse sensing located only at the tip of the needle embedded into a programmable bevel-tip needle modeled through 3-D space curves [43].

In this article, we validate our needle shape-sensing model through needle insertion experiments over various insertion scenarios including single- and double-layer tissues, along with S-shaped needle insertions. A four-active area needle is inserted into artificial tissues under stereo vision to provide 3-D ground truth measurements of the needle shape during insertion. In Section II, we present our models for FBG curvature sensing and shape-sensing methods. Section III discusses our experimental setup and methods to perform automated needle insertion using 3-D stereo visualization. Finally, the results are presented in Section IV and a discussion of these results in Section V. The novelty of our work includes the presentation of a novel Lie-group theoretic approach to 3-D needle shape-sensing for S-shaped insertions and 3-D needle shape-sensing using a four-active area needle in multilayered tissue and S-shaped insertions over varying insertion depths using 3-D ground truth measurements under stereo vision.

II. SHAPE MODELS AND METHODS

A. FBG Sensor Model

FBGs are Bragg reflectors inscribed in fiber-optic cables which are able to detect strain and temperature shifts by the change in the Bragg wavelength. This change in the peak Bragg wavelength is characterized by Bragg's law and the shift in the Bragg wavelength, $\Delta\lambda$, can be approximated by

$$\Delta\lambda = k_\epsilon \epsilon + k_T \Delta T \quad (1)$$

where ϵ is the strain induced in the FBG, ΔT is the change in temperature of the FBG, and k_ϵ and k_T are the characteristic constants of the FBG associated with strain and temperature, respectively [37].

In our FBG-sensorized needle, at each of the active areas, we have three FBGs arranged in a trigonal pattern array (120° relative to each other) as seen in Fig. 1. In order to measure the

effect of strain directly, we remove the effect of temperature by performing *temperature compensation*. Inspired by [44] and assuming that k_T is the same for all of the FBGs (validated by temperature tests of these FBGs), we can perform temperature compensation by subtracting the mean Bragg wavelength shift from each of FBGs in their associated array, called an *active area*, thus eliminating temperature change effects on the Bragg wavelength shift since FBGs in an active area are aligned with each other and should thus experience the same local temperature change. We define this method as *temperature compensation*.

For a rod modeled as an Euler-Bernoulli rod, we can determine the curvature of the rod by

$$\kappa = \frac{\epsilon}{R} \quad (2)$$

where κ is the curvature at some radius R from the rod's center. We observe that, with temperature compensation, $\Delta\lambda \propto \kappa$. Leveraging this proportionality, a linear model is used to compute the cross-sectional curvature $\omega = (\kappa_{xz}, \kappa_{yz})^T$ (z -axis is perpendicular to the needle's cross-sectional area) from the temperature compensated wavelength shifts of an FBG active area, $\overline{\Delta\lambda}_i$ ($i = 1, 2, 3$), by

$$\omega = (\kappa_{xz} \ \kappa_{yz})^T = C (\overline{\Delta\lambda}_1 \ \overline{\Delta\lambda}_2 \ \overline{\Delta\lambda}_3)^T \quad (3)$$

where $C \in \mathbb{R}^{2 \times 3}$ is the calibration matrix, determined by the FBG-sensorized needle calibration process.

B. Needle Shape-Sensing

The sensor-based Lie-group theoretic model [31] describes the curvature (ω_1 and ω_2 along the local x - and y -axes, respectively) and torsion (ω_3 along the local z -axis) of the needle as

$$\omega(s) = [\omega_1 \ \omega_2 \ \omega_3]^T = \left(R^T(s) \frac{dR(s)}{ds} \right)^\vee \quad (4)$$

where $R(s) \in SO(3)$ denotes the rotation matrix in 3-D space describing the orientation of the body-fixed frame attached at each point along the needle. $s \in [0, L]$ denotes the arc length of the needle with total insertion depth L . The \vee operation defines a 3-D vector associated with a 3×3 skew-symmetric matrix $R^T(dR/ds)$ [32].

When inserting into tissue, the needle is modeled as an inextensible elastic rod. Under ideal conditions, we assume that the needle experiences uniformly distributed loads. In case of homogeneous tissue (i.e., single-layer) insertion, a single uniformly distributed load is assumed. In all cases, due to an asymmetric bevel tip, the needle ideally deforms only in one plane (yz plane in the world frame as shown in Fig. 2), which is captured by introducing the intrinsic curvature $\kappa_0(s)$. For the single-layer case, an intrinsic curvature coefficient, κ_c , is introduced to model the combined effect of the needle's and tissue's mechanical properties on needle bending. Note that the intrinsic curvature coefficient, κ_c , is included in the definition of intrinsic curvature to remove the physical modeling of the needle-tissue interaction, later to be determined in a sensor-based optimization, allowing for flexible application of this model since it does not require task-specific knowledge

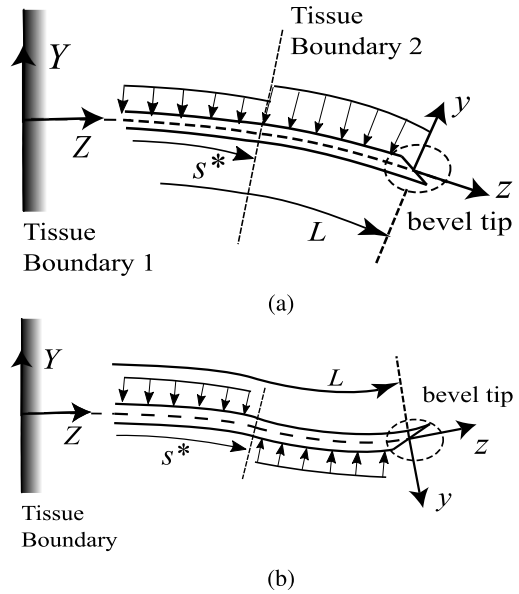


Fig. 2. Schematic of the bevel-tipped needle in the ideal C-shaped insertion into two-layered tissue (tissue 1 and tissue 2) and S-shaped insertion into single-layered tissue, which are modeled as two different uniformly distributed loads (normal components are only shown). (a) Two-layer C-shaped model. (b) S-shaped model.

of needle insertion mechanics. The intrinsic curvature of a single-layer case insertion is given by

$$\kappa_0(s) = \kappa_c \left(1 - \frac{s}{L} \right)^2. \quad (5)$$

We also consider double-layer C-shaped insertion and single-layer S-shaped insertion scenarios in this experiment. To properly accommodate these scenarios, we use different intrinsic curvature functions to allow for the proper beam mechanics to be realized. We determined these models by deriving the form of the curvature parameterized over the length of the needle by modeling uniformly distributed loads associated with the different scenarios.

For the double-layer case, we define the length of the needle that is inside the first layer to be s^* and associate two intrinsic curvature coefficients as $\kappa_{c,1}$ and $\kappa_{c,2}$ for the first and second layers, respectively, as seen in Fig. 2(a). $\kappa_0(s)$ for the double-layer C-shaped case is given by

$$\kappa_0(s) = \begin{cases} \kappa_{c,1} \left(\frac{s^* - s}{L} \right)^2 + \kappa_{c,2} \left(1 - \frac{s^*}{L} \right) \left(1 + \frac{s^*}{L} - \frac{2s}{L} \right) & (0 \leq s \leq s^*) \\ \kappa_{c,2} \left(1 - \frac{s}{L} \right)^2 & (s^* \leq s \leq L). \end{cases} \quad (6)$$

Previous work has extended the intrinsic curvature formulation for the three-layer case in [31].

For the single-layer S-shaped insertion, the needle is rotated 180° about its axis, at some insertion depth, s^* , seen in Fig. 2(b). This induces a point of inflection in the needle shape caused by the inversion of the curvature, from the change in the needle's bevel-tip's orientation. Therefore, similar to the

single-layer C-shaped insertion, we define $\kappa_0(s)$ for the single-layer S-shaped insertion to be

$$\kappa_0(s) = \begin{cases} \kappa_c \left(\frac{s^*}{L}\right)^{2/3} (1 - \frac{s}{L})^2, & 0 < s < s^* \\ \frac{\kappa_c}{2} \left(\left(\frac{s^*}{L}\right)^{2/3} - \left(\frac{L-s^*}{L}\right)^{2/3} \right), & s = s^* \\ -\kappa_c \left(\frac{L-s^*}{L}\right)^{2/3} (1 - \frac{s}{L})^2, & s^* < s \leq L. \end{cases} \quad (7)$$

Equation (7) allows for the unbalancing of net force over the needle by using a proportionality factor with respect to the length of the needle prior to the point of inflection and afterward. Here the factor of $2/3$ was used as an approximative modeling based on simulations of the dependence of κ_c with respect to the insertion depth in [45]. The reason why $\kappa_0(s) < 0$ for $s > s^*$ in (7) is as follows. Mathematically, the true body-fixed angular deformation vector after the rotation, denoted as ω' , is obtained as

$$\omega' = \text{Ad}(R_z(180^\circ)) \omega = R_z(180^\circ) \omega$$

where R_z denotes the rotation matrix about the z -axis, and $\text{Ad}(\cdot)$ denotes the adjoint operator on the rotation group [32]. Since ω always parallel to $\mathbf{e}_1 = [1 \ 0 \ 0]^T$, 180° axial rotation results in the change of sign. At the point of rotation, $s = s^*$, there is a nontrivial intrinsic curvature. The reason for this is to model the deviation at the point of inflection modeled in [46]. This formulation can easily be extended to model general axial needle rotation cases.

Intrinsic curvature in this model provides a reference to which the actual needle deformation will follow. Minimizing the elastic potential energy of the rod

$$\mathcal{V} = \int_0^L \frac{1}{2} (\omega - \omega_0)^T B (\omega - \omega_0) ds \quad (8)$$

enables the determination of needle deformation $\omega(s)$ and the body-fixed orientation $R(s)$ along the needle shaft. Specifically, the minimization of the equation yields the Euler-Poincaré equation [47], [48] as

$$\frac{d}{ds} [B(\omega - \omega_0)] + \omega \times B(\omega - \omega_0) = \mathbf{0} \quad (9)$$

which will be solved together with (4). Here, B is stiffness matrix of the needle including the bending and torsional stiffnesses, and $\omega_0 = [\kappa_0 \ 0 \ 0]^T$. Finally, the needle shape, $\mathbf{r}(s)$, can be determined by integrating $R(s)$ by

$$\mathbf{r}(s) = \int_0^s R(\sigma) \mathbf{e}_3 d\sigma \quad (10)$$

where $\mathbf{e}_3 = [0 \ 0 \ 1]^T$.

Finally, this approach is combined with FBG sensor information to determine the necessary optimization variables through the optimization of the cost function, (11), with FBG measurement data. An array of optimization variables, η , includes the initial value of ω , denoted as ω_{init} , and the intrinsic curvature coefficients associated with each layer of tissue, $\kappa_{c,i}$ ($i = 1, 2$)

$$\mathcal{C}(\eta) = \sum_{j=1}^m \left\{ \left(\omega_{j,1}^m - \omega_1(s_j) \right)^2 + \left(\omega_{j,2}^m - \omega_2(s_j) \right)^2 \right\} \quad (11)$$

where $\omega_{j,1}^m$ and $\omega_{j,2}^m$ denote the curvature data from the FBGs (m is the number of FBGs). This optimization is performed using the interior-point nonlinear optimization algorithm [49].

C. 3-D Needle Shape Reconstruction

Stereo vision is used to measure the 3-D ground truth needle shape in the following experiments. Stereo camera calibration is performed to remove distortion and determine the stereo camera setup's intrinsic and extrinsic parameters. 3-D stereo needle shape reconstruction is as follows. First, the needle centerline is determined using an image of the current needle shape and a reference image prior to the insertion of the needle. The reference image is subtracted from the current image to highlight the needle for needle segmentation. Through a series of techniques are used to segment the highlighted needle in each of the stereo images and the needle centerline is determined in each of the individual images. After determining the centerline of the needle, stereo image rectification is performed, followed by smoothing and interpolating the centerlines using second-order B-splines. Stereo matches are determined by template matching at each of the centerline points along the epipolar lines on resized images by $2.5\times$, and are smoothed and interpolated by second-order B-splines. Second-order B-splines were used for their flexibility in complex curve fitting, along with stability [50]. Finally, triangulating the interpolated stereo matches is used to reconstruct the 3-D needle shape.

III. EXPERIMENTS

The goal of the needle insertion experiment presented in this article is to validate our needle shape-sensing model.

A. FBG-Sensorized Needle

We built a four-active area FBG-sensorized needle, where the FBG-sensing arrays are placed in a trigonal pattern (120° relative angle) at the sensing locations of 10, 30, 65, and 100 mm from the tip of an 18G nitinol MRI-compatible needle (type KIM18/20, Innovative Tomography Products GmbH, Germany), as shown in Fig. 1. We chose to build a needle with only four active areas to balance our model's requirement for accurate curvature estimation along the needle's length and device accessibility through reducing the cost of materials since FBG fibers are more expensive as additional active areas are added to the fiber. These sensing locations were chosen to distribute the curvature sensing along the needle's insertion length for better approximation of our model's parameters, $\kappa_c, \omega_{\text{init}}$.

B. Needle Characterization and Calibration

Sensorized needle characterization is performed to ensure the assumptions of linearity between the FBG sensor readings and the strain induced in each of the fibers after construction of the needle. During construction of the needle, fabrication errors can arise from the fiber-optic cable twisting inside the grooves of the needle or an improper adherence to the needle at the sensing location. Needle characterization is performed by using an XYZ linear stage (XYR-6060 & LM-400, Dover

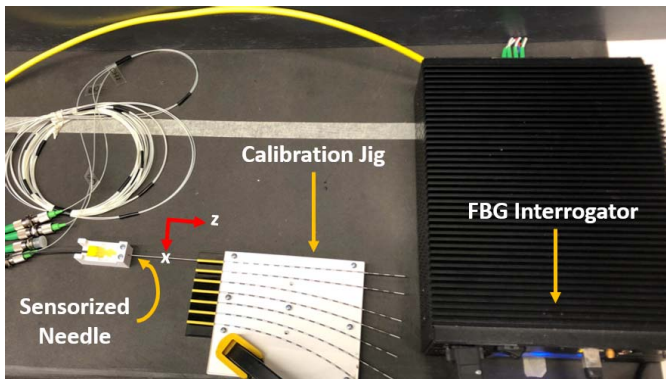


Fig. 3. Needle calibration using constant curvature jig setup.

Motion, Boxborough, MA, USA) robot with a motorized rotary stage (B5990TS, Velmex, Inc., Bloomfield, NY, USA) to rotate the needle about its axis. At the tip of the needle, deflections are induced at $\leq 10\%$ to remain in an Eulerian approximation of strain induced in the needle. Five trials are performed for three different rotation angles (0° , 120° , and -120°) at ten deflections at the tip recording 200 FBG signal shifts per deflection loading and unloading the beam. The three different rotation angles are aimed to maximize the strain induced in each of the fibers individually.

Needle calibration was performed using constant curvature jigs to map the temperature compensated wavelength shifts at each of the sensing locations in the sensorized needle. Fig. 3 illustrates the experimental setup for the sensorized needle calibration. Two 3-D-printed jigs (material ABS, Stratasys F170 printer) with a total of 13 distinct curvatures ranging from 0 to 4 m^{-1} were used to induce constant curvatures in the four-active areas along the needle. These grooves were filled with 16G needles for the needle to be inserted into, reducing human error of needle orientation when placing the needle into the grooves. We gathered the 200 FBG signal responses using a Micron Optics Hyperion si155 optical sensing interrogator, providing a wavelength resolution of 1 pm. Temperature compensation's efficacy was evaluated by inserting the needle into the constant curvature jigs while in an incubator, evaluating the needle's ability to reproduce the same curvature at varying temperatures using the temperature-compensated wavelengths and room-temperature calibration.

For calibration, the needle was bent in the xz and yz planes referenced in Fig. 2, inserted into the each of the constant curvature grooves five times for four different orientations at angles 90° from each other (0° , 90° , 180° , and -90°). The calibration matrices, C , for each active area from (3) are then determined by a weighted least squares problem where non-clinically relevant curvatures ($> 1 \text{ m}^{-1}$) are weighted 1/20th the weight of the clinically relevant curvatures ($\leq 1 \text{ m}^{-1}$) [51]. The 12 nonzero curvatures are partitioned into a calibration and validation datasets to determine the validity of our calibration. After performing curvature calibration, reliability weightings, w_i , are given to each of the four-active areas such that $\sum_{i=1}^4 w_i = 1$, and that $\{w_i\}$ are to optimize the deviation of needle's determined shape from FBG measurements from

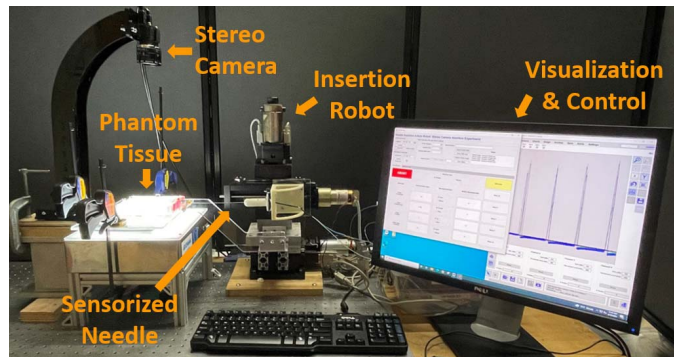


Fig. 4. Needle insertion experimental setup under stereo visualization. Insertion of the needle into the gel phantom is performed.

ground truth in the constant curvature cases. These weightings allow for optimal shape-sensing capabilities given our model. The calibration errors of this needle's shape-sensing capabilities are given by a mean RMSE of 0.196 mm for all the clinically relevant curvatures.

C. Experimental Setup

Isotropic gel phantoms are constructed from plastic of various stiffness (Plastic from M-F Manufacturing Company, TX, USA) to simulate soft and stiff tissues. To create the stiff tissue, a ratio of 4:1 liquid plastic to plastic hardener was used and to create the soft tissue, no plastic hardener was used. To construct the two-layer gel tissue, the first tissue is poured and cooled into our phantom layer mold using a divider to control the size of the first layer. The divider is then removed and the molten second layer is poured into the remaining volume of the mold, remelting the boundary of the first layer, gluing the two layers together. The optical sensing interrogator was used to gather FBG sensor data and the experiment is visualized under stereo vision. An acrylic box of dimensions allowing for 120 mm insertion depths holds the tissue in-place and staples at the insertion side of the gel are placed to prevent excess tissue deformation at the insertion boundary, simulating the clinician stretching the tissue during initial insertion. A 3-D-printed needle holder is attached to a manual rotary stage installed on a 4-degree of freedom linear stage to perform the needle insertion. A custom 18G needle guide is attached to the base of the needle insertion robot listed in Fig. 4 to ensure that insertions into the phantom tissue are nearly perpendicular to the tissue boundary. A custom, funnel-shaped needle guide for 18G needles placed at the end of an acrylic arm ensures perpendicularity of the needle to the phantom box and straight insertions into tissue.

For each of the tissues, nine quasi-static insertion trials are performed for insertion depths from 30 to 120 mm in 15 mm increments. These insertion depths are chosen to evaluate the shape-sensing accuracy over the various insertion depths. The needle sensors are, first, calibrated in a straight needle jig by collecting 200 unstrained FBG wavelengths. To provide a reference image pair for needle segmentation, prior to each insertion trial, a stereo image pair is taken. At each of the insertion depths, a pair of stereo images

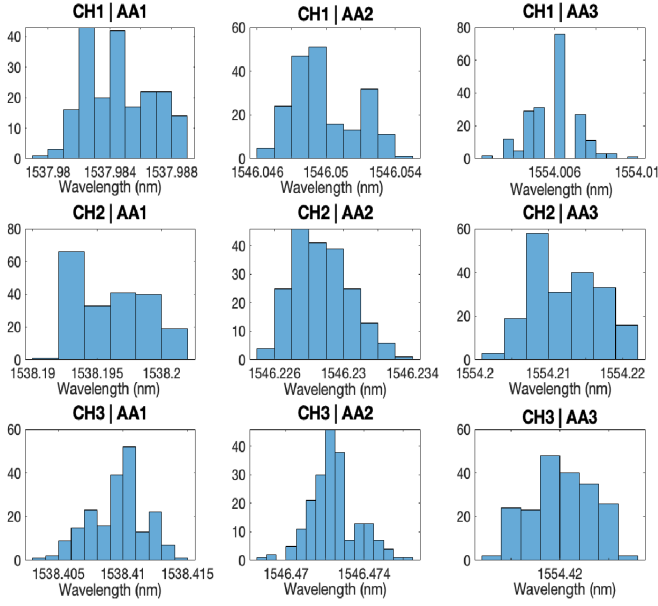


Fig. 5. Histogram of 200 normally distributed FBG wavelength samples from an insertion trial, indexed by channel (CH) and active area (AA) for the four active area FBG-sensorized needles. Active areas 1–3 are shown here as characteristic examples of the normal distribution of FBG wavelength peaks.

along with 200 wavelengths per FBG sensor is collected to serve as our ground truth and shape-sensing information. About 200 wavelength samples are taken per FBG to ensure a normal distribution of samples that are captured to represent a proper mean of the sampled FBG wavelength, as seen in Fig. 5. Bragg wavelength shifts are calculated by taking the difference of the mean strained and unstrained wavelengths, followed by temperature compensation to be incorporated in the shape-sensing model and determine the 3-D needle shape. The ground truth needle shape is reconstructed from the stereo pair of images following the method in Section II-C. The tip of the needle is used as a feature point to align the needle shapes from FBG shape-sensing and stereo reconstruction, as it is reliably segmented and matched in the stereo image pair and a point-cloud registration registers the needle insertion shapes as seen in the image reprojections of Figs. 7 and 8 with the stereo reconstruction in green and the FBG-sensed needle shape in red.

For visualization of the needle, two identical cameras (Flea2 FL2-0852C, Point Grey Research Inc., Richmond, BC, Canada) were used for stereo reconstruction. The resolution of each of the cameras was 1024×768 pixels. The shape reconstruction method in Section II-C was evaluated on needles inserted into constant curvature jigs and has a mean 3-D reconstruction error of 0.160 ± 0.055 mm.

IV. RESULTS

Three types of 3-D shaped error metrics were considered: root-mean-square error (RMSE), in-bending-plane (yz) error (IPE), and out-of-bending-plane (xz) error (OPE). RMSE characterizes the overall shape-reconstruction accuracy, and IPE quantifies the error contribution in the natural bending

TABLE I
CALIBRATION ERROR FROM CURVATURE CALIBRATION FOR THE VALIDATION CURVATURES AND THE ASSOCIATED ACTIVE AREA RELIABILITY WEIGHTING

Active Area	Curvature Error (1/mm)	Reliability Weight
1	0.16 ± 0.11	0.216
2	0.15 ± 0.11	0.683
3	0.34 ± 0.24	0.075
4	0.47 ± 0.39	0.025

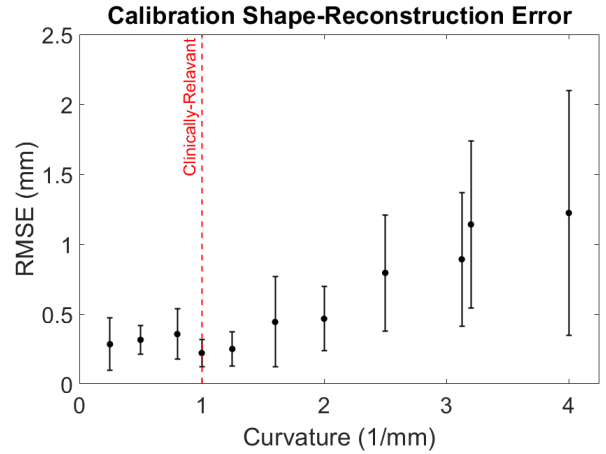


Fig. 6. Calibration reconstruction error. The curvatures before the red-dashed line are considered to be clinically relevant curvatures.

plane of the bevel-tipped needle and OPE with deflections out of the natural bending plane of the bevel-tipped needle. RMSE is defined between two 3-D needle shapes $\{\mathbf{r}_1(s_i)\}_{i=1}^N$ and $\{\mathbf{r}_2(s_i)\}_{i=1}^N$ as

$$\text{RMSE} = \sqrt{\frac{1}{N} \sum_{i=1}^N \|\mathbf{r}_1(s_i) - \mathbf{r}_2(s_i)\|^2} \quad (12)$$

where s_i is the parameterized arc length of each of the two needle shapes. The IPE is defined as

$$\text{IPE} = \frac{1}{N} \sum_{i=1}^N \|(\mathbf{0} \ 1 \ 1) \cdot (\mathbf{r}_1(s_i) - \mathbf{r}_2(s_i))\|. \quad (13)$$

Similarly, OPE is defined as

$$\text{OPE} = \frac{1}{N} \sum_{i=1}^N \|(\mathbf{1} \ 0 \ 1) \cdot (\mathbf{r}_1(s_i) - \mathbf{r}_2(s_i))\|. \quad (14)$$

A. Needle Characterization and Calibration

Needle curvature calibration was performed and the results of the curvature calibration are presented in Table I. Here, we can see that the curvature measurements for active areas 1 and 2 are shown to be the most reliable with active area 4 being the least. This results in active area 4's reliability weighting to be much smaller than the rest, sensibly so since the strain experienced at the needle tip is smaller than those further from the tip.

The needle shape reconstruction error from the curvature calibrations is presented in Fig. 6, where the mean and standard deviations of the curvatures are plotted against the

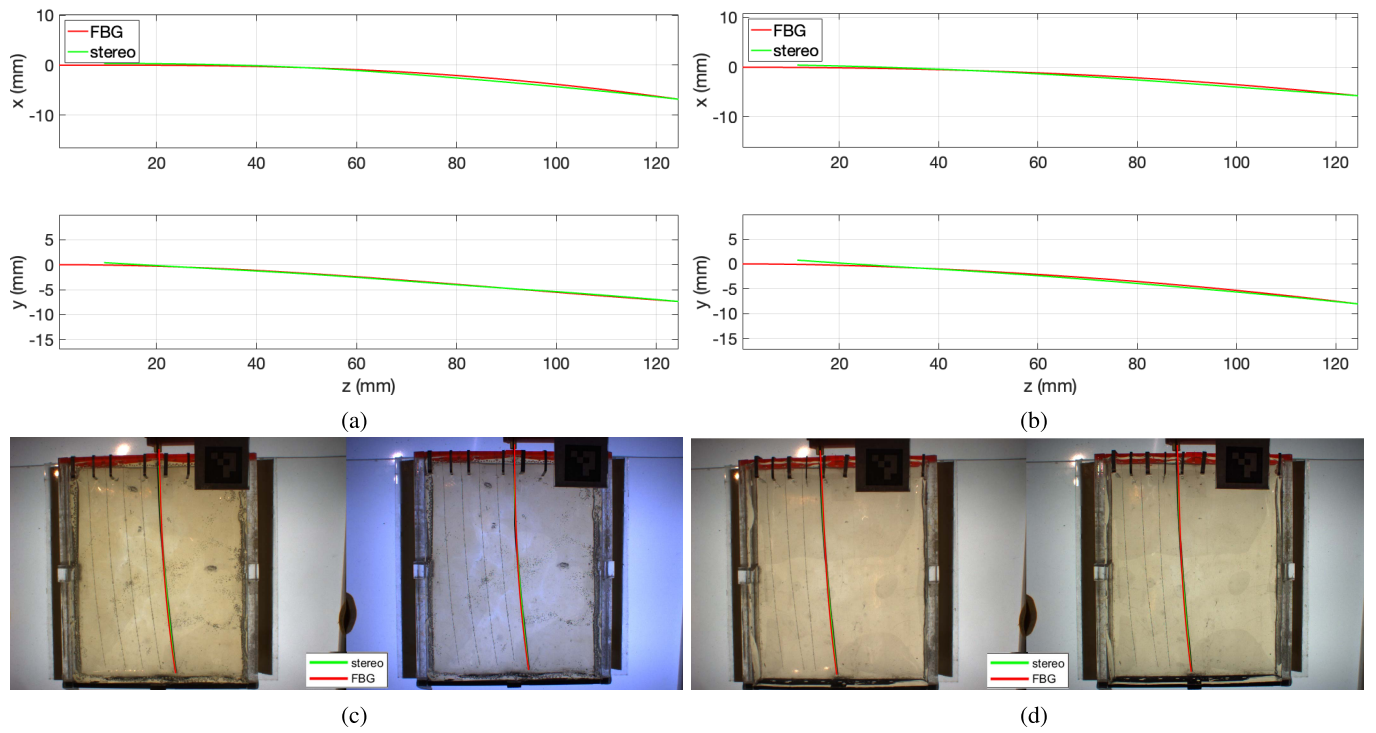


Fig. 7. 3-D shape-sensing overlaid with stereo reconstruction of the needle shape inserted into single-layer tissue for C-shaped insertion. (a) 3-D shape: hard tissue (30 shore units). (b) 3-D shape: soft tissue (20 shore units). (c) Image reprojection: hard tissue (30 shore units). (d) Image reprojection: soft tissue (20 shore units).

constant curvature of the needle. Notably, the shape-sensing error increases with the increase in curvature as well as the variation in our shape reconstruction. However, errors are within less than 0.5 mm on average in the clinically relevant realm of curvatures and the calibration is thus considered sufficient.

B. Shape-Sensing Results

Insertion experiment results are reported for the insertion scenarios of: single-layer C-shaped, single-layer S-shaped, and double-layer C-shaped insertions for soft and hard layer tissues. In Fig. 7, we see that in both hard and soft phantom tissues, we achieve good correspondence between the FBG shape-sensing results and the stereo ground truth measurements exemplified in the 3-D needle shapes and image reprojections.

In Fig. 8, we inserted our sensorized needle into soft-hard and hard-soft tissue configurations to evaluate our shape-sensing accuracy. We see that the deflections are similar for both the soft-hard and the hard-soft tissue configurations and that both shape-sensing results overlap well with the stereo ground truth in the 3-D needle shapes and the image reprojections.

In Fig. 9, the point of inflection was at the insertion depth of 65 mm so the first half of needle insertion was C-shaped insertion and the second half of the insertion was S-shaped. Notably, the deflection in hard tissue was greater than the deflection in soft tissue. This makes sense since there would be more force exerted on the needle for the hard tissue insertion scenario. Furthermore, we saw from the 3-D needle shapes

and the image reprojections that the shape-sensing aligned well with the ground truth stereo needle shape for both tissues.

Error statistics are determined over all of the insertion trials for each insertion depth and for each of the different shape-sensing scenarios. In Fig. 10(a), we can see that the errors associated with shape-sensing over varying insertion depths for all insertion trials are consistent with mean values of RMSE, IPE, and OPE all hovering less than 0.5 mm. In total, the data we collected contains 650 needle shapes to reproduce with few outliers observed in the shape-sensing error statistics. We observed larger shape-sensing errors from the hard-soft tissue C-shaped insertions. We note that these errors were largely attributed to the motion of the hard-soft tissue boundary while the needle entered the second layer. This deviation induced modeling errors for measurements of s^* in (6). Furthermore, the movement of the tissue boundary induced small artifacts in our stereo visualization, yielding reconstruction errors. Therefore, we are confident that these outliers seen are due to measurement and visualization errors during insertion. In Fig. 10(b), we can see the shape-sensing performs well in varying insertion scenarios, single- and multilayer alike. All of our errors hover relatively less than 0.5 mm with a slightly larger, but accounted for, error seen from the hard-soft insertion scenario.

V. DISCUSSION

The shape-sensing model here meets the requirement of 0.5 mm shape-reconstruction error for prostate needle intervention, given from Table II that most of the errors are less than 0.5 mm. There is an exception at 105 mm insertion depth

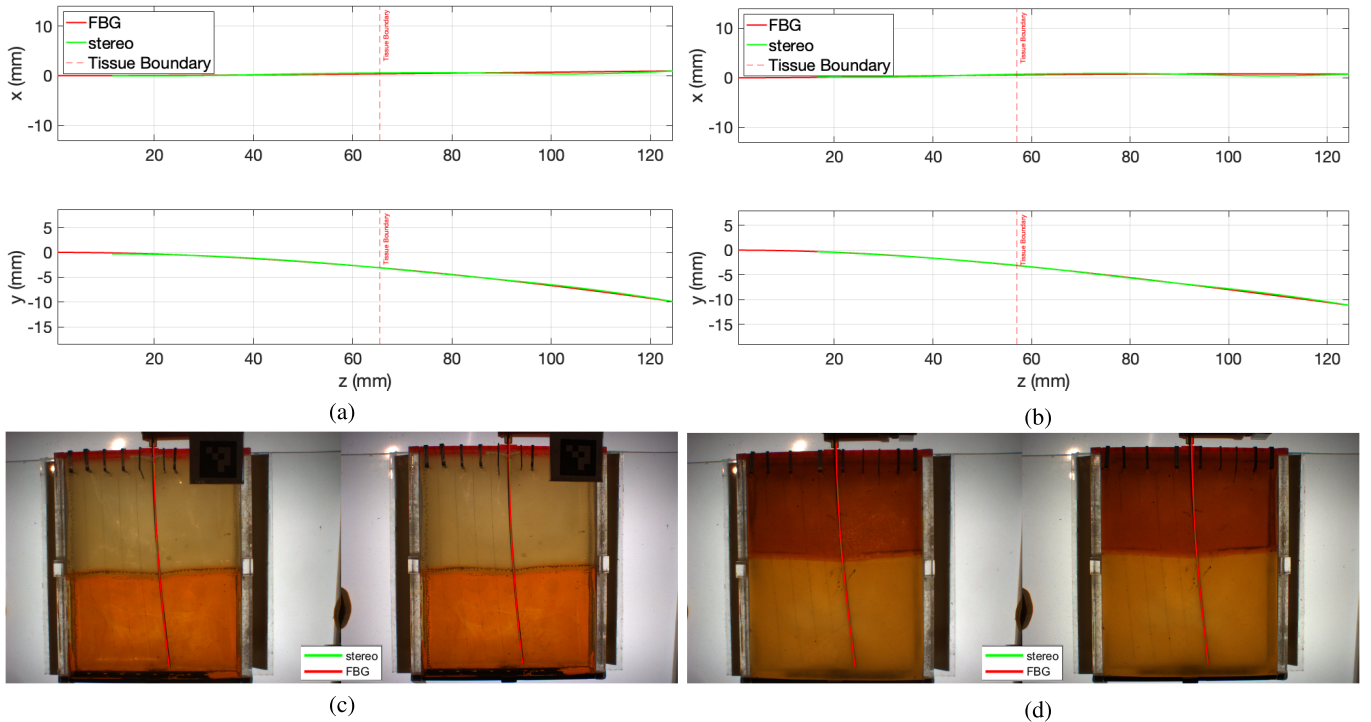


Fig. 8. 3-D shape-sensing overlaid with stereo reconstruction of the needle shape inserted into double-layer tissue for C-shaped insertion. (a) 3-D shape soft-hard tissue (20–30 shore units). (b) 3-D shape hard-soft tissue (30–20 shore units). (c) Image reprojection: soft-hard tissue (20–30 shore units). (d) Image reprojection: hard-soft tissue (30–20 shore units).

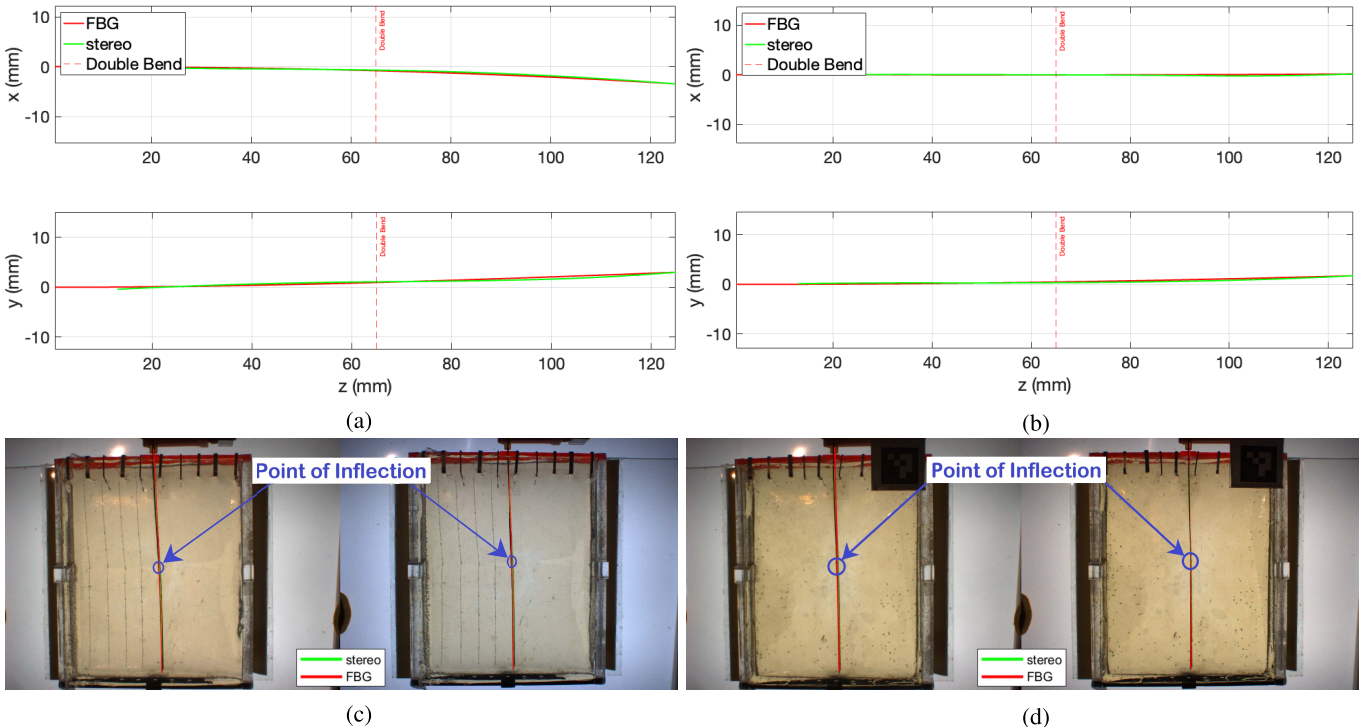


Fig. 9. 3-D shape-sensing overlaid with stereo reconstruction of the needle shape inserted into single-layer tissue for S-shaped insertion. (a) 3-D shape hard tissue (30 shore units). (b) 3-D shape soft tissue (20 shore units). (c) Image reprojection: hard tissue (30 shore units). (d) Image reprojection: soft tissue (20 shore units).

for the hard-soft tissue; however, we found that this error is caused by a few outlier insertions that had poor visualization of the needle tip causing for errors in the stereo reconstruction,

hence the large mean RMSE and STD. However, we find that rest of our shape-sensing results is fairly uniform over all insertion depths and all needle shape scenarios. This could also

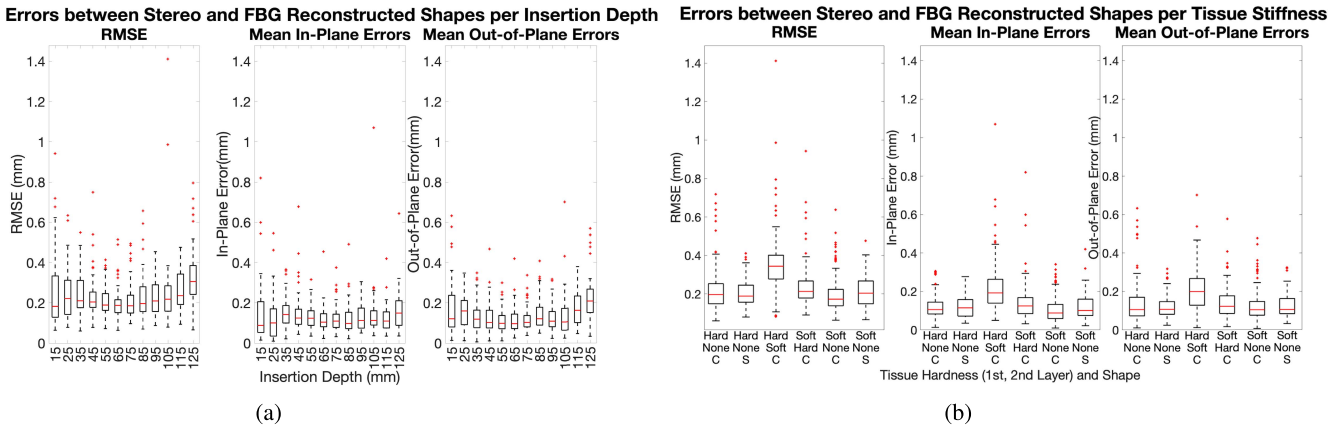


Fig. 10. Shape-sensing error distributions over the varying insertion scenarios and insertion depths. (a) Per insertion depth. (b) Per experiment.

TABLE II
SHAPE-SENSING RMSE ERROR STATISTICS PER INSERTION SCENARIO OVER THE VARYING INSERTION DEPTH

Insertion Depth (mm)	Mean of RMSE \pm STD of RMSE (mm)					
	C-Shape				S-Shape	
	Soft	Hard	Soft-Hard	Hard-Soft	Soft	Hard
15	0.269 \pm 0.111	0.261 \pm 0.184	0.423 \pm 0.269	0.226 \pm 0.126	N/A	N/A
25	0.259 \pm 0.105	0.195 \pm 0.077	0.276 \pm 0.100	0.369 \pm 0.183	N/A	N/A
35	0.229 \pm 0.098	0.198 \pm 0.060	0.242 \pm 0.097	0.379 \pm 0.097	N/A	N/A
45	0.196 \pm 0.035	0.199 \pm 0.078	0.210 \pm 0.032	0.403 \pm 0.170	N/A	N/A
55	0.179 \pm 0.052	0.192 \pm 0.050	0.205 \pm 0.027	0.324 \pm 0.076	N/A	N/A
65	0.173 \pm 0.054	0.342 \pm 0.111	0.175 \pm 0.029	0.191 \pm 0.031	N/A	N/A
75	0.133 \pm 0.028	0.218 \pm 0.093	0.166 \pm 0.043	0.377 \pm 0.093	0.196 \pm 0.068	0.174 \pm 0.034
85	0.176 \pm 0.057	0.215 \pm 0.068	0.278 \pm 0.167	0.377 \pm 0.122	0.169 \pm 0.061	0.178 \pm 0.039
95	0.160 \pm 0.039	0.216 \pm 0.116	0.221 \pm 0.081	0.345 \pm 0.055	0.217 \pm 0.078	0.193 \pm 0.032
105	0.155 \pm 0.045	0.194 \pm 0.082	0.218 \pm 0.059	0.518 \pm 0.403	0.204 \pm 0.071	0.225 \pm 0.092
115	0.223 \pm 0.067	0.232 \pm 0.113	0.209 \pm 0.055	0.316 \pm 0.107	0.280 \pm 0.125	0.281 \pm 0.105
125	0.410 \pm 0.137	0.454 \pm 0.155	0.256 \pm 0.042	0.384 \pm 0.222	0.277 \pm 0.097	0.229 \pm 0.082

be caused by the needle-tissue interaction in the second layer of the tissue (depths > 65 mm). The interaction between the tissue and the needle's second active area could cause variation in the needle shape, as it is near the tissue boundary at and after 105 mm. This can cause variable strains in the active area, causing larger errors for determining the parameters of the second layer. Notably, this effect appears to be more dominant in the hard-soft insertion as from the soft-hard insertion. Finally, we see that there are larger errors at 125 mm for all of the insertions. At 125 mm, the needle tip is near the edge of the acrylic box containing the tissue, so the active areas could be strained significantly by causing for increased tissue pressures as the tissue is pushed against the boundary of the box. This effect is also particularly noticeable in the soft-tissue C-shaped insertion case where the IPE is much larger at 125, potentially due to the increased elasticity noted from the softer tissue. An interesting future work would be to consider this boundary effect in performing the shape-sensing by the consideration of the viscoelastic properties of the tissue.

Table III compiles the current state-of-the-art methods for shape-sensing in needles and catheters. The fiber structure listed for these devices contains the number of fiber-optic channels used, the type of FBG core structure (i.e., single-core or multicore) and in parentheses the total number of FBGs in the device. The table contains the device evaluated for shape-sensing using either a single-core fiber or multicore

fiber with the number of fibers and sensing points over all of the fibers used for shape-sensing. This table also contains the model used for shape-sensing, the evaluation medium and shape-type, along with a presented error from the referenced publication. Multiple papers are listed for different configurations of their experiments for proper evaluation across all methods. Notably, as compared to other methods, our needle contains one of the smallest number of FBGs over all of the methods with the exception of Donder and Baena [43], Henken et al. [26], and Roesthuis et al. [33]. Here, Henken et al. [26] used half the number of AAs than our method and resulted in errors on a magnitude of six times as great for 2-D shape-sensing errors, however, uses a longer needle than ours. Roesthuis et al. [33] utilized a similar sensing structure as ours for a longer needle and achieved as our system for C-shape and S-shape, evaluating a kinematic-based model with shape-sensing errors in 2-D. For Donder and Baena [43], they used a Kalman filtering at the single sensing points they are performing in order to reconstruct the entire needle shape, updating points of along the needle as the sensors pass through them. For the single sensing point at the tip, they achieve errors much larger than what we have observed for the C-shape and S-shape for needle reconstruction, as well as about 2–3 times as reconstruction errors for their C-shaped and S-shaped insertion into tissue with using eight insertion points for a similar needle to our own. Catheter shape-sensing

TABLE III
STATE-OF-THE-ART SHAPE-SENSING METHOD COMPARISON TABLE (ALL UNITS IN mm)

Authors	Device	Fiber Structure	Length	Model	Medium	Shape	Error Type	Error
Lezcano, et al.*	Needle	3 Single-core (12)	125	Lie-Group	Phantom Tissue	C-Shape	RMSE (3D)	0.25 ± 0.14
Lezcano, et al.*	Needle	3 Single-core (12)	125	Lie-Group	Phantom Tissue	C-Shape	Max (3D)	0.50 ± 0.33
Lezcano, et al.*	Needle	3 Single-core (12)	125	Lie-Group	Phantom Tissue	S-Shape	RMSE (3D)	0.22 ± 0.08
Lezcano, et al.*	Needle	3 Single-core (12)	125	Lie-Group	Phantom Tissue	S-Shape	Max (3D)	0.40 ± 0.14
Henken, et al. [26]	Needle	3 Single-core (6)	172	Frenet-Serret	Free Space	C-Shape	Tip (2D)	1.32 ± 0.48
Roesthuis, et al. [33]	Needle	3 Single-core (12)	172	Kinematics-based	Phantom Tissue	C-Shape	Max (2D)	0.57 ± 0.02
Roesthuis, et al. [33]	Needle	3 Single-core (12)	172	Kinematics-based	Phantom Tissue	S-Shape	Max (2D)	0.53 ± 0.04
Roesthuis, et al. [33]	Needle	3 Single-core (12)	172	Kinematics-based	Phantom Tissue	Out-of-Plane	Max (2D)	0.68 ± 0.04
Abayazid, et al. [34]	Needle	3 Single-core (12)	185	Mechanics-based	Phantom Tissue	C-Shape	Tip (3D)	1.5 ± 0.8
Abayazid, et al. [34]	Needle	3 Single-core (12)	185	Mechanics-based	Phantom Tissue	S-Shape	Tip (3D)	2.0 ± 0.7
Abayazid, et al. [34]	Needle	3 Single-core (12)	185	Mechanics-based	Phantom Tissue	Out-of-Plane	Tip (3D)	2.1 ± 1.1
Khan, et al. [36]	Catheter	4 Multi-core (24)	118	Frenet-Serret	Free Space	C-Shape	Mean (3D)	0.22 ± 0.12
Khan, et al. [38]	Catheter	4 Multi-core (32)	103	Bishop Frames	Free Space	C-Shape	Tip (3D)	0.09 ± 0.03
Khan, et al. [38]	Catheter	4 Multi-core (32)	103	Bishop Frames	Free Space	S-Shape	Tip (3D)	1.01 ± 0.09
Khan, et al. [38]	Catheter	4 Multi-core (32)	103	Bishop Frames	Gelatin	3D Curve	Tip (3D)	1.94 ± 0.05
Al-Ahmad, et al. [37]	Catheter	7 Multi-core (72)	115	Frenet-Serret	3D-Printed Curves	3D Curve	Max (3D)	2.84 ± 0.82
Jacke, et al. [40]	Catheter	7 Multi-core (266)	380	Frenet-Serret	Free Space	C-Shape	Mean (3D)	0.45 ± 0.09
Jacke, et al. [40]	Catheter	7 Multi-core (266)	380	Frenet-Serret	Free Space	S-Shape	Mean (3D)	0.81 ± 0.30
Jacke, et al. [40]	Catheter	7 Multi-core (266)	380	Frenet-Serret	3D-Printed Vessel	3D Curve	Mean (3D)	1.13**
Jacke, et al. [41]	Catheter	7 Multi-core (266)	380	Frenet-Serret	Free Space	C-shape	Mean (3D)	0.51**
Jacke, et al. [41]	Catheter	7 Multi-core (266)	380	Frenet-Serret	Free Space	S-shape	Mean (3D)	0.62**
Jacke, et al. [41]	Catheter	7 Multi-core (266)	380	Frenet-Serret	Free Space	3D Curve	Mean (3D)	0.63**
Donder, et al. [43]	Needle	4 Multi-core (4)	120	Kalman Filter	Phantom Tissue	C-Shape	Tip (3D)	2.03 ± 1.33
Donder, et al. [43]	Needle	4 Multi-core (4)	120	Kalman Filter	Phantom Tissue	3D Curve	Tip (3D)	3.08 ± 1.70
Donder, et al. [43]	Needle	4 Multi-core (4)	120	Kalman Filter	Phantom Tissue	S-Shape	Tip (3D)	2.24 ± 1.54
Donder, et al. [43]	Needle	4 Multi-core (4)	120	Kalman Filter	Real Tissue	C-Shape	Tip (3D)	4.69 ± 1.37
Donder, et al. [43]	Needle	4 Multi-core (4)	120	Kalman Filter	Real Tissue	3D Curve	Tip (3D)	5.42 ± 1.91
Donder, et al. [43]	Needle	4 Multi-core (4)	120	Kalman Filter	Real Tissue	S-Shape	Tip (3D)	5.60 ± 2.70
Donder, et al. [43]	Needle	4 Multi-core (56)	120	Kalman Filter	Phantom Tissue	C-Shape	Tip (3D)	1.01 ± 0.51
Donder, et al. [43]	Needle	4 Multi-core (56)	120	Kalman Filter	Phantom Tissue	S-Shape	Tip (3D)	1.95 ± 0.98
Donder, et al. [43]	Needle	4 Multi-core (56)	120	Kalman Filter	Phantom Tissue	3D Curve	Tip (3D)	2.18 ± 1.30
Donder, et al. [43]	Needle	4 Multi-core (56)	120	Kalman Filter	Real Tissue	C-Shape	Tip (3D)	1.16 ± 0.64
Donder, et al. [43]	Needle	4 Multi-core (56)	120	Kalman Filter	Real Tissue	S-Shape	Tip (3D)	2.04 ± 1.01
Donder, et al. [43]	Needle	4 Multi-core (56)	120	Kalman Filter	Real Tissue	3D Curve	Tip (3D)	2.87 ± 1.63

*This refers to the results presented in this current work.

**Statistics on repeated measurements were not reported nor able to be calculated.

is a difficult problem as large bending angles and torsion can affect the reconstruction efficacy. All of these models used some 3-D curve frame methods for shape-sensing and dense placement of AAs over the length of the device. These shape-sensing methods require some method for interpolating curvature over the length of the device, which can cause for instabilities in the shape-sensing in the Khan et al. [36], [38] present two methods of shape reconstruction, one using Frenet–Serret equations and the other using parallel transport frames. Small errors were achieved in their C-shaped experiment for free space, but errors grew larger with the complexity of their shape. Al-Ahmad et al. [37] used Frenet–Serret equations leveraging MCFs for torsion compensation to evaluate shape-sensing accuracy in 3-D curves, achieving comparable errors to Khan et al. [36], [38] in gelatin. Jackle et al. [40], [41] evaluated shape-sensing over a much longer catheter, achieving impressive shape-sensing results, but required many AAs in order to reconstruct the entire needle shape. In comparison with our model, we find that as the complexity of the needle shape increases, our shape-sensing errors remain static. Through using prior information of the type of shape we are inducing in the needle, we are able to use a mechanics-informed method for accurate curvature interpolation over sparse sensing locations to fit our current curvature information through the needle’s FBGs. These results illustrate the novelty, efficacy, and accuracy of our sensor-based

shape-sensing model, allowing for accurate shape-sensing in diverse insertion scenarios with sparse sensing.

VI. CONCLUSION

In this article, we experimentally validated a Lie-group theoretic 3-D shape-sensing model over varying insertion depths, needle shapes, and tissue configurations. C-shaped single-layer, C-shaped double-layer, and S-shape single-layer insertion scenarios are considered over varying insertion depths up to 125 mm. We rigorously validated our shape-sensing method by inserting a four active area sensorized FBG needle into soft, hard, and combination tissues using a robotic insertion platform imaged using stereo vision. Stereo reconstructions of the needle were used as a 3-D ground truth of the needle shape and were compared to the Lie-group theoretic modeling of the needle shape captured by the needle’s FBG sensors. Stereo reconstruction of the needle was validated using a constant curvature jig and is found to have mean reconstruction error of 0.160 ± 0.055 mm. Our shape reconstruction accuracy observed for all experiments were 0.240 ± 0.131 mm over all of the 650 insertions performed in this experiment indicating adequate performance of our shape-sensing method under rigorous testing. We also discussed the benefits of using a Lie-group theoretic approach to needle shape-sensing through a comparison of the current state-of-the-art methods. Lie-group theoretic shape-sensing enables sparse sensing modalities to

perform accurate needle shape-sensing over varying insertion depths, maintaining shape-reconstruction errors for diverse needle insertion scenarios. The use of our Lie-group theoretic approach to shape-sensing in real insertion scenarios intends to leverage a combination of the presented models and these models' extensions depending on the model which best matches the present insertion's needle configuration. Limitations of this work include longer insertions greater than 125 mm and evaluation in real tissue. Further experimentation could be performed with modifications to our experimental setup in order to accommodate longer needle insertion scenarios. Future work includes experimental validation of shape-sensing in real tissue, extending our model to accommodate shape-prediction over varying insertion depths and stochastic modeling of our needle shape.

ACKNOWLEDGMENT

The authors thank Alexandra Cheng for their contribution in assisting the analysis of their many insertion trials.

REFERENCES

- [1] C. H. Pernar, E. M. Ebot, K. M. Wilson, and L. A. Mucci, "The epidemiology of prostate cancer," *Cold Spring Harbor Perspect. Med.*, vol. 8, no. 12, 2018, Art. no. a030361.
- [2] B. R. Matlaga, L. A. Eskew, and D. L. McCullough, "Prostate biopsy: Indications and technique," *J. Urol.*, vol. 169, pp. 12–19, Jan. 2003.
- [3] S. Okazawa, R. Ebrahimi, J. Chuang, S. E. Salcudean, and R. Rohling, "Hand-held steerable needle device," *IEEE/ASME Trans. Mechatronics*, vol. 10, no. 3, pp. 285–296, Jun. 2005.
- [4] R. J. Roesthuis, N. J. van de Berg, J. J. van den Dobbelenstein, and S. Misra, "Modeling and steering of a novel actuated-tip needle through a soft-tissue simulant using fiber Bragg grating sensors," in *Proc. IEEE Int. Conf. Robot. Autom. (ICRA)*, May 2015, pp. 2283–2289.
- [5] N. Shahriari, R. J. Roesthuis, N. J. van de Berg, J. J. van den Dobbelenstein, and S. Misra, "Steering an actuated-tip needle in biological tissue: Fusing FBG-sensor data and ultrasound images," in *Proc. IEEE Int. Conf. Robot. Autom. (ICRA)*, May 2016, pp. 4443–4449.
- [6] J. A. Engh, G. Podnar, S. Y. Khoo, and C. N. Riviere, "Flexible needle steering system for percutaneous access to deep zones of the brain," in *Proc. IEEE 32nd Annu. Northeast Bioeng. Conf.*, Apr. 2006, pp. 103–104.
- [7] T. K. Adebar, A. E. Fletcher, and A. M. Okamura, "3-D ultrasound-guided robotic needle steering in biological tissue," *IEEE Trans. Biomed. Eng.*, vol. 61, no. 12, pp. 2899–2910, Dec. 2014.
- [8] R. J. Webster, J. S. Kim, N. J. Cowan, G. S. Chirikjian, and A. M. Okamura, "Nonholonomic modeling of needle steering," *Int. J. Robot. Res.*, vol. 25, nos. 5–6, pp. 509–525, 2006.
- [9] D. Glozman and M. Shoham, "Image-guided robotic flexible needle steering," *IEEE Trans. Robot.*, vol. 23, no. 3, pp. 459–467, Jun. 2007.
- [10] X. Tan, Y. Lee, C.-B. Chng, K.-B. Lim, and C.-K. Chui, "Robot-assisted flexible needle insertion using universal distributional deep reinforcement learning," *Int. J. Comput. Assist. Radiol. Surg.*, vol. 15, no. 2, pp. 341–349, Feb. 2020.
- [11] W. Park, J. Seob Kim, Y. Zhou, N. J. Cowan, A. M. Okamura, and G. S. Chirikjian, "Diffusion-based motion planning for a nonholonomic flexible needle model," in *Proc. IEEE Int. Conf. Robot. Autom.*, Apr. 2005, pp. 4600–4605.
- [12] S. P. DiMaio and S. E. Salcudean, "Needle steering and motion planning in soft tissues," *IEEE Trans. Biomed. Eng.*, vol. 52, no. 6, pp. 965–974, Jun. 2005.
- [13] J. Xu, V. Duindam, R. Alterovitz, and K. Goldberg, "Motion planning for steerable needles in 3D environments with obstacles using rapidly-exploring random trees and backtracking," in *Proc. IEEE Int. Conf. Autom. Sci. Eng.*, Aug. 2008, pp. 41–46.
- [14] H. Su, M. Zervas, G. A. Cole, C. Furlong, and G. S. Fischer, "Real-time MRI-guided needle placement robot with integrated fiber optic force sensing," in *Proc. IEEE Int. Conf. Robot. Autom.*, May 2011, pp. 1583–1588.
- [15] X. Tan, P. Yu, K.-B. Lim, and C.-K. Chui, "Robust path planning for flexible needle insertion using Markov decision processes," *Int. J. Comput. Assist. Radiol. Surg.*, vol. 13, no. 9, pp. 1439–1451, Sep. 2018.
- [16] V. Duindam, R. Alterovitz, S. Sastry, and K. Goldberg, "Screw-based motion planning for bevel-tip flexible needles in 3D environments with obstacles," in *Proc. IEEE Int. Conf. Robot. Autom.*, May 2008, pp. 2483–2488.
- [17] Y. J. Zhao, W. Q. Wu, Y. D. Zhang, R. X. Wang, J. C. Peng, and Y. Yu, "3D dynamic motion planning for robot-assisted cannula flexible needle insertion into soft tissue," *Int. J. Adv. Robotic Syst.*, vol. 13, no. 3, pp. 1–11, 2016, doi: [10.5772/64199](https://doi.org/10.5772/64199).
- [18] M. Li, D. Gao, Y. Lei, and T. Xu, "Dynamic path planning for bevel-tip flexible needle insertion into soft tissue based on a real-time finite element model," *Math. Problems Eng.*, vol. 2020, pp. 1–13, Jul. 2020.
- [19] R. Seifabadi, I. Iordachita, and G. Fichtinger, "Design of a teleoperated needle steering system for MRI-guided prostate interventions," in *Proc. 4th IEEE RAS EMBS Int. Conf. Biomed. Robot. Biomechatronics (BioRob)*, Jun. 2012, pp. 793–798.
- [20] R. Seifabadi, E. E. Gomez, F. Aalamifar, G. Fichtinger, and I. Iordachita, "Real-time tracking of a bevel-tip needle with varying insertion depth: Toward teleoperated MRI-guided needle steering," in *Proc. IEEE/RSJ Int. Conf. Intell. Robots Syst.*, Nov. 2013, pp. 469–476.
- [21] Y. L. Park et al., "Real-time estimation of 3-D needle shape and deflection for MRI-guided interventions," *IEEE/ASME Trans. Mechatronics*, vol. 15, no. 6, pp. 906–915, Dec. 2010.
- [22] N. Abolhassani and R. Patel, "Deflection of a flexible needle during insertion into soft tissue," in *Proc. Int. Conf. IEEE Eng. Med. Biol. Soc.*, Aug. 2006, pp. 3858–3861.
- [23] K. R. Henken, J. Dankelman, J. J. van den Dobbelenstein, L. K. Cheng, and M. S. van der Heiden, "Error analysis of FBG-based shape sensors for medical needle tracking," *IEEE/ASME Trans. Mechatronics*, vol. 19, no. 5, pp. 1523–1531, Oct. 2014.
- [24] L. Guinot, R. Tsumura, S. Inoue, and H. Iwata, "Development of a needle deflection detection system for a CT guided robot," in *Proc. IEEE/SICE Int. Symp. Syst. Integr. (SII)*, Jan. 2020, pp. 34–38.
- [25] S. Song, Z. Li, H. Yu, and H. Ren, "Electromagnetic positioning for tip tracking and shape sensing of flexible robots," *IEEE Sensors J.*, vol. 15, no. 8, pp. 4565–4575, Aug. 2015.
- [26] K. K. Henken, D. Van Gerwen, J. Dankelman, and J. Van Den Dobbelenstein, "Accuracy of needle position measurements using fiber Bragg gratings," *Minimally Invasive Therapy Allied Technol.*, vol. 21, no. 6, pp. 408–414, 2012.
- [27] R. Secoli and F. Rodriguez y Baena, "Closed-loop 3D motion modeling and control of a steerable needle for soft tissue surgery," in *Proc. IEEE Int. Conf. Robot. Autom.*, May 2013, pp. 5831–5836.
- [28] M. Khadem, B. Fallahi, C. Rossa, R. S. Sloboda, N. Usmani, and M. Tavakoli, "A mechanics-based model for simulation and control of flexible needle insertion in soft tissue," in *Proc. IEEE Int. Conf. Robot. Autom. (ICRA)*, May 2015, pp. 2264–2269.
- [29] M. Khadem, C. Rossa, R. S. Sloboda, N. Usmani, and M. Tavakoli, "Mechanics of tissue cutting during needle insertion in biological tissue," *IEEE Robot. Autom. Lett.*, vol. 1, no. 2, pp. 800–807, Jul. 2016.
- [30] S. Jiang and X. Wang, "Mechanics-based interactive modeling for medical flexible needle insertion in consideration of nonlinear factors," *J. Comput. Nonlinear Dyn.*, vol. 11, no. 1, Jan. 2016, Art. no. 011004, doi: [10.1115/1.4030747](https://doi.org/10.1115/1.4030747).
- [31] J. S. Kim, M. Chatrasiingh, S. Kim, J. Suthakorn, and I. I. Iordachita, "Fiber Bragg grating based needle shape sensing for needle steering system: Evaluation in inhomogeneous tissue," in *Proc. IEEE SENSORS*, Oct. 2017, pp. 1–3.
- [32] G. S. Chirikjian and A. B. Kyatkin, *Harmonic Analysis for Engineers and Applied Scientists*. New York, NY, USA: Dover, 2016.
- [33] R. J. Roesthuis, M. Kemp, J. J. van den Dobbelenstein, and S. Misra, "Three-dimensional needle shape reconstruction using an array of fiber Bragg grating sensors," *IEEE/ASME Trans. Mechatronics*, vol. 19, no. 4, pp. 1115–1126, Aug. 2014.
- [34] M. Abayazid, M. Kemp, and S. Misra, "3D flexible needle steering in soft-tissue phantoms using fiber Bragg grating sensors," in *Proc. IEEE Int. Conf. Robot. Autom.*, May 2013, pp. 5843–5849.
- [35] N. J. van de Berg, J. Dankelman, and J. J. van den Dobbelenstein, "Design of an actively controlled steerable needle with tendon actuation and FBG-based shape sensing," *Med. Eng. Phys.*, vol. 37, no. 6, pp. 617–622, Jun. 2015, doi: [10.1016/j.medengphy.2015.03.016](https://doi.org/10.1016/j.medengphy.2015.03.016).
- [36] F. Khan, A. Denasi, D. Barrera, J. Madrigal, S. Sales, and S. Misra, "Multi-core optical fibers with Bragg gratings as shape sensor for flexible medical instruments," *IEEE Sensors J.*, vol. 19, no. 14, pp. 5878–5884, Jul. 2019.

- [37] O. Al-Ahmad, M. Ourak, J. Van Roosbroeck, J. Vlekken, and E. Vander Poorten, "Improved FBG-based shape sensing methods for vascular catheterization treatment," *IEEE Robot. Autom. Lett.*, vol. 5, no. 3, pp. 4687–4694, Jul. 2020.
- [38] F. Khan, A. Donder, S. Galvan, F. R. Y. Baena, and S. Misra, "Pose measurement of flexible medical instruments using fiber Bragg gratings in multi-core fiber," *IEEE Sensors J.*, vol. 20, no. 18, pp. 10955–10962, Sep. 2020.
- [39] O. Al-Ahmad, M. Ourak, J. Vlekken, and E. Vander Poorten, "FBG-based estimation of external forces along flexible instrument bodies," *Frontiers Robot. AI*, vol. 8, pp. 1–12, Jul. 2021.
- [40] S. Jäckle, T. Eixmann, H. Schulz-Hildebrandt, G. Hüttmann, and T. Pätz, "Fiber optical shape sensing of flexible instruments for endovascular navigation," *Int. J. Comput. Assist. Radiol. Surg.*, vol. 14, no. 12, pp. 2137–2145, Dec. 2019, doi: [10.1007/s11548-019-02059-0](https://doi.org/10.1007/s11548-019-02059-0).
- [41] S. Jäckle et al., "3D catheter guidance including shape sensing for endovascular navigation," *Proc. SPIE*, vol. 11315, Mar. 2020, Art. no. 1131504.
- [42] A. Amantayeva, N. Adilzhanova, A. Issatayeva, W. Blanc, C. Molardi, and D. Tosi, "Fiber optic distributed sensing network for shape sensing-assisted epidural needle guidance," *Biosensors*, vol. 11, no. 11, p. 446, Nov. 2021.
- [43] A. Donder and F. R. Y. Baena, "Kalman-filter-based, dynamic 3-D shape reconstruction for steerable needles with fiber Bragg gratings in multicore fibers," *IEEE Trans. Robot.*, vol. 38, no. 4, pp. 2262–2275, Aug. 2022.
- [44] A. Issatayeva, A. Amantayeva, W. Blanc, C. Molardi, and D. Tosi, "Temperature compensation of the fiber-optic based system for the shape reconstruction of a minimally invasive surgical needle," *Sens. Actuators A, Phys.*, vol. 329, Oct. 2021, Art. no. 112795, doi: [10.1016/j.sna.2021.112795](https://doi.org/10.1016/j.sna.2021.112795).
- [45] D. A. Lezcano, I. I. Iordachita, and J. S. Kim, "Trajectory generation of FBG-sensorized needles for insertions into multi-layer tissue," in *Proc. IEEE SENSORS*, Oct. 2020, pp. 1–4.
- [46] M. Li, G. Li, B. Gonenc, X. Duan, and I. Iordachita, "Towards human-controlled, real-time shape sensing based flexible needle steering for MRI-guided percutaneous therapies," *Int. J.*, vol. 2014, pp. 211–215, Jan. 2006.
- [47] D. D. Holm, J. E. Marsden, and T. S. Ratiu, "The Euler–Poincaré equations and semidirect products with applications to continuum theories," *Adv. Math.*, vol. 137, pp. 1–81, Jul. 1998.
- [48] J. S. Kim and G. S. Chirikjian, "Conformational analysis of stiff chiral polymers with end-constraints," *Mol. Simul.*, vol. 32, no. 14, pp. 1139–1154, Dec. 2006.
- [49] A. S. Nemirovski and M. J. Todd, *Interior-Point Methods for Optimization*, vol. 17. 2008.
- [50] B. Pham, "Quadratic B-splines for automatic curve and surface fitting," *Comput. Graph.*, vol. 13, no. 4, pp. 471–475, Jan. 1989. [Online]. Available: <https://linkinghub.elsevier.com/retrieve/pii/0097849389900083>
- [51] L. Zhang et al., "A new method for fiber Bragg grating based needle shape sensing calibration," in *Proc. IEEE Int. Conf. Robot. Biomimetics (ROBIO)*, Dec. 2019, pp. 1953–1958.



Dimitri A. Lezcano received the B.A. degree in physics and mathematics from the McDaniel College, Westminster, MD, USA, in 2019, and the M.S.E. degree in robotics from Johns Hopkins University, Baltimore, MD, USA, 2021, where he is currently pursuing the Ph.D. degree in mechanical engineering.

His research interests include computer-integrated surgical technologies, including flexible needle shape-sensing, needle trajectory generation, and flexible needle steering.



Julian I. Iordachita (Senior Member, IEEE) received the M.Eng. degree in industrial robotics and the Ph.D. degree in mechanical engineering from the University of Craiova, Craiova, Romania, in 1989 and 1996, respectively.

In 2000, he was a Postdoctoral Fellow with the Brady Urological Institute, School of Medicine, Johns Hopkins University, Baltimore, MD, USA, and from 2002 to 2003, he was a Research Fellow with the Graduate School of Frontier Sciences, The University of Tokyo, Tokyo, Japan.

He is currently a Research Professor in mechanical engineering and robotics with the Johns Hopkins University. His research interests include medical robotics, image guided surgery with a specific focus on microsurgery, interventional MRI, smart surgical tools, and medical instrumentation.



Jin Seob Kim (Member, IEEE) received the M.S. degree in mechanical engineering from Seoul National University, Seoul, South Korea, in 2000, and the M.S. and Ph.D. degrees in mechanical engineering from Johns Hopkins University, Baltimore, MD, USA, in 2004 and 2006, respectively.

He was an Assistant Research Professor in mechanical engineering and robotics with Johns Hopkins University, where he is currently a Senior Lecturer in mechanical engineering and robotics.

He did postdoctoral work at the Johns Hopkins Institute for NanoBioTechnology, the Johns Hopkins Bloomberg School of Public Health, and Johns Hopkins University. His research interests include medical robotics, in particular, sensor-based mathematical modeling of continuum robots, computational modeling of biological systems, and application of noncommutative harmonic analysis.